Performance Evaluation of hi-k Lung-inspired 3D-printed Polymer Heat Exchangers

Behzad Ahmadi, Sajjad Bigham [*]

Department of Mechanical Engineering-Engineering Mechanics, Michigan Technological University, 1400 Townsend Drive, Houghton, MI 49931-1295, USA

ABSTRACT

Polymer heat exchangers are attractive thermal management solutions due to their low-cost, lightweight, anti-fouling, and anti-corrosion characteristics. They, however, demonstrate poor thermal characteristics mainly due to the low thermal conductivities of typical polymers. Additive manufacturing of high thermal conductivity polymer heat exchangers utilizing complex heat transfer topologies could potentially address the issue. In this study, thermal performances of 3D-printed polymer heat exchangers with intricate internal geometries including a lung-inspired design at low-to-high thermal conductivities are experimentally and numerically examined. It was found the effective thermal conductivity of a 3D-printed polymer heat exchanger is close to the through-plane thermal conductivity. It was also identified that through-plane leakage in thin 3D-printed polymer walls is a major challenge associated with 3D-printed polymer heat exchangers. The issue was remedied by in-situ infusion of an epoxy layer during the 3D-printing and a post-curing process. Experiments conducted at various thermo-hydraulic conditions showed that the high thermal conductivity lung-inspired polymer heat exchanger offers high thermal duties at reduced pressure drop penalties and exceptionally high effectiveness of 70–80% that is comparable to that of metal-based heat exchangers. At an air Reynolds number of 1200, the volume-based power density of the high thermal conductivity lung-inspired design is 522 kW/m^3, which is a 101% improvement compared with a typical plate-and-frame design. This study concludes that the thermal performance of a polymer heat exchanger strongly depends on both material (i.e., thermal conductivity) and architecture (i.e., an optimum design with a minimal thermal resistance between hot and cold sides). Insights gained from this study could offer new pathways for designing innovative 3D-printed polymer heat exchanger technologies with unprecedented heat transfer rates at reduced pressure drop penalties for lightweight, anti-fouling, and/or anti-corrosion applications.

1. Introduction

Polymer heat exchangers (PHXs) are considered a promising alternative to metal heat exchangers for several critical applications, including but not limited to electric vehicles, desalination plants, seawater treatment facilities, chemical units, air conditioning systems, dehydration systems, and air-cooled power plants [1–5] [27] [28]. The low weight of PHXs is attractive for battery and electronic thermal management of electric vehicles. The low surface energy and antifouling characteristics of PHXs are beneficial to heat exchangers employed in water treatment and desalination plants, particularly at high salinity levels [29]. The anti-corrosion properties of PHXs are appealing for acidic and chlorinated environments in chemical processing [6]. More recently, 3D-printed polymer heat exchangers were employed to

improve the cooling of windings in electric machines [7] and thermal management of high power density Li-ion batteries for electric vehicles [8]. Additionally, polymers have low melting and processing temperatures, thereby leading to more cost-effective heat exchanger solutions.

Despite the above advantages, PHXs suffer from a low thermal conductivity range compared with metal HXs [9]. Typical polymers offer thermal conductivities on the order of 0.1 W/m-K, which is two to three orders of magnitude lower than that of common metallic heat exchanger materials, including stainless steel and aluminum. The low thermal conductivity of PHXs could be addressed by restructuring the polymer chains toward an ideal crystallinity fiber [10] or employing polymer composite materials, including metal-filled polymers and carbon nanotube (CNT) composites [11–16]. A study conducted by Glade et al. [17] showed that thermal conductivity of composites could increase up to 13

~ 20 W/m-K, which is approximately two orders of magnitude higher than that of typical polymers and comparable with stainless steel. Cevallos et al. [18] developed a Nylon 12 polymer composite webbed-tube heat exchanger for a gas–liquid heat exchanger. The effective thermal conductivity of the polymer composite estimated inversely by determining the discrepancy between empirical and numerical data was found to equal approximately 1.8 W/m-K. The observed thermal performance was about 1.65 times higher than that of a heat exchanger employing unenhanced polymer walls. A metal-polymer composite HX with V-shape micro-grooves explored by Sun et al. [19] showed a thermal dissipation performance similar to that of a commercially available aluminum HX. A PHX designed by Trojanowski et al. [20] for condensing boiler applications showed that a thermally conductive PHX with a thermal conductivity of 2.5 W/m-K is adequate to achieve an effectiveness similar to a stainless steel heat exchanger. However, the above polymer HXs are primarily based upon conventional manufacturing approaches and thus bound by their inherent limitations.

The thermal performance and compactness of polymer HXs can be substantially improved if advanced heat transfer topologies are employed. Particularly, as noted by Jabbour et al. [21], the low conductivity of polymeric materials could be compensated by optimization of geometric HX parameters to reach performances similar to those of a compact metallic HX. These geometries, however, are often complex and cannot be easily realized by conventional manufacturing techniques. Additive manufacturing enables to fabricate complex heat transfer features for next-generation polymer HXs. This is particularly relevant for polymer HXs due to their low processing temperatures and thus cost-effective manufacturing. Felber et al. [22] examined the performance of an air-cooled 3D-printed Acrylonitrile Butadiene Styrene (ABS) polymer heat exchanger fabricated using the Fused Deposition Modeling (FDM) method. Their results showed that the thermal duty of a polymer HX increases with thermal conductivity in a nonlinear manner. They concluded that efforts to enhance the printability of small polymer features and thin walls should be conducted alongside improving polymer thermal conductivity. Arie et al. [23] explored a PHX made of 150 μm-thick high-density polyethylene thin sheets using layer-by-layer line welding with a laser through an additive manufacturing process. They concluded that the wall thermal resistance, which typically is a limiting factor for PHXs, accounted for only 3% of the total thermal resistance for this very thin wall HX. In another study, Arie et al. [24] examined an additively manufactured cross-flow composite metal-polymer HX fabricated using Fused Filament Fabrication (FFF). Here, high conductivity metal fiber fins were employed to directly connect the hot and cold sides, thus minimizing the wall resistance. Their results showed up to 220% and 125% improvement in heat flow rate over mass and volume, respectively, compared to state-of-the-art plate fins HX configurations. However, these 3D-printed PHXs still employ a low conductivity polymer material and relatively simple heat transfer geometries.

In this study, it is demonstrated that the thermal performance of PHXs can be substantially improved if a high thermal conductivity (i.e., hi-k) polymer is 3D-printed in the form of a lung-inspired topology. The thermal performance of the hi-k lung-inspired PHX is compared against three plate-and-frame PHXs designs with low to high thermal conductivities. In the following, first, details of the 3D-printed PHXs and the experimental test loop facility are discussed. Then, the simulation procedure is explained. Finally, measured and simulated thermal performance values are discussed at different thermo-hydraulic conditions.

2. Polymer heat exchanger design and 3D-printing

In this study, three plate-and-frame and one lung-inspired PHXs were 3D-printed and experimentally evaluated. The HXs were made of Polylactic acid (i.e., PLA), metal-filled PLA with 33% copper powder content (i.e., M−PLA), and a hi-k nylon-based polymer (TC Poly Inc.). The hi-k nylon-based polymer has a nominal in-plane thermal conductivity of 4 W/m-K and a through-plane thermal conductivity of 1 W/m-K. It should

be noted that the thermal conductivity of the base PLA and nylon polymers are 0.13 and 0.25 W/m-K, respectively. The PHXs were 3D-printed using the Fused Deposition Modeling (FDM) technique. The FDM, also known as Fused Filament Fabrication (FFF), is a widely used additive manufacturing (AM) technique due to its low-cost and high printing speed. In this technique, the desired object is 3D-printed by deposition of a melted filament extruded through a hot nozzle layer by layer. Additionally, the maximum processing temperature of the three examined polymer filaments was less than 290 °C, thereby allowing less energy-intensive and thus cost-effective manufacturing of next-generation HXs with complex and enhanced heat transfer topologies compared with metal-based fabrication methods, including metal 3D-printing.

The plate-and-frame PHXs were designed in a counter-flow arrangement, as shown in Fig. 1a-d. The core heat exchanger design includes two layers with an overall dimension of $10 \times 5 \times 0.5$ cm^3. Each layer consists of 25 channels with a length of 68 mm and a cross-section area of 1×1 mm^2. Early versions of the 3D-printed PLA, M−PLA, and hi-k nylon-based PHXs showed a through-plane leakage in which small air bubbles periodically appeared in the liquid flow stream. The leakage issue was remedied by in-situ infusion of an epoxy layer during the 3D-printing process, as shown in Fig. 1b. The 3D-printed PHXs were then post-cured to enable a leakage-free HX design.

The hi-k nylon-based lung-inspired PHX was fabricated to evaluate the thermal performance of a complex polymer topology that is only achievable through the 3D-printing method. The main idea behind the proposed HX topology is to provide an intimate contact area between hot and cold flow streams with reduced thermal resistance. This goal could be potentially realized when the hot and cold flow streams are volumetrically co-distributed through each other, thereby maximizing the surface-area-to-volume ratio. Such an HX design resembles the bronchi architecture of a human lung, exhibiting an improved flow distribution for an efficient heat transfer process. In practice, several manufacturing limitations should be considered to realize such an HX design through the FDM technique. First, the representative cell serving as the base structure is simplified to feature a trifurcating network of channels (cf. Fig. 1f) demonstrating three converging inlet and diverging outlet pathways each of which at a different 3D spatial orientation. The trifurcating network of channels allows volumetric co-distribution of the hot and cold flow streams and is simple enough to be 3D-printed through the FDM technique. Second, the solid 3D-printed walls separating the hot and cold flow streams should establish a zero through-plane leakage upon treatment. After 3D-printing and assessing several wall thicknesses of the trifurcating network, a 1-mm wall thickness was found suitable. And, third, the FDM method typically requires internal supports for the 3D-printing of complex objects with large overhangs. However, the proposed HX design does not allow easy removal of the 3D-printed internal supports due to its unique intertwined flow networks. Therefore, several lung-inspired HX designs with different cell-scale dimensions and angles were 3D-printed and optimized for structural integrity in the absence of any internal support during the 3D-printing process. As a result, a cell-scale HX design utilizing dimensions and angles shown in Fig. 1f was found suitable for the FDM technique. It should be noted that a 3D-printing method with higher quality than the FDM approach and/or a more careful parametric optimization of the HX geometry could increase the surface-area-to-volume ratio of the lung-inspired HX design, thereby potentially improving the overall HX performance.

Fig. 1e shows images of the hi-k lung-inspired 3D-printed PHX, including a schematic of a representative cell serving as the base structure. As shown, each base structure has three converging inlet pathways and three diverging outlets each of which at a different 3D spatial orientation. Fig. 1e also shows a 3D cross-sectional view of the lung-inspired 3D-printed PHX. As shown, the design employs two intertwined bicontinuous fluid networks for efficient heat transfer between hot and cold sides at a reduced pressure drop penalty. The first network (i.e., the red color) volumetrically divides an incoming air
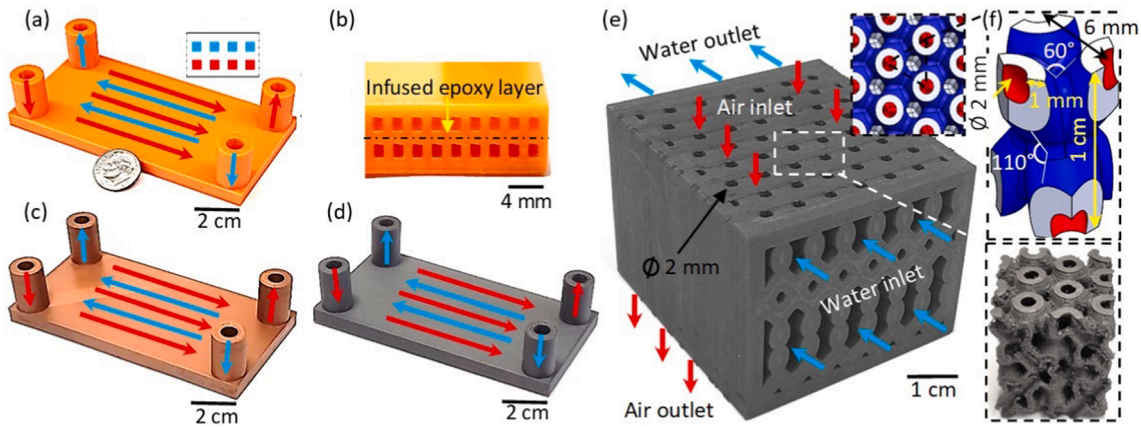
Fig. 1. 3D-printed PHXs: (a) the plate-and-frame PLA HX, (b) a cross-sectional view of the PLA HX, (c) the plate-and-frame M−PLA HX, (d) the plate-and-frame hi-k nylon-based PHX, and (e) the lung-inspired hi-k nylon-based PHX.

stream into multiple connected curved channels that are spread out within the second water-cooled network for a reduced thermal resistance between hot air and cold water sides. Additionally, the first network continuously splits and then mixes the hot air stream for an enhanced air-side heat transfer process. The second network (i.e., the blue color) distributes the cooling water within and through the first network. Therefore, it is envisioned the lung-inspired PHX design outperforms its plate-and-frame counterparts due to (i) its excellent volumetric flow distribution with a minimal thermal resistance between hot air and cold water sides at reduced pressure drop penalties and (ii) continuous mixing within the air side with an enhanced air-side heat transfer coefficient. The overall dimensions of the lung-inspired PHX are $4.3 \times 4.1 \times 3.2$ cm^3. Additionally, the air side consists of 52 inlet/outlet ports with a 2 mm inlet diameter. The thickness of the wall separating air and water streams is similar to that of the plate-and-frame PHXs (i.e., 1 mm).

3. Test loop facility and uncertainty analysis

3.1. Experimental test setup

Fig. 2 shows a schematic and an actual image of the heat exchanger test loop facility to evaluate thermo-hydraulic characteristics of the 3D-printed PHXs. The test facility was equipped with a liquid micro-pump (Model: Hydra Cell P300) and an air compressor both controlled by variable frequency drives (VFDs) to circulate the working fluids. As discussed in the abstract and introduction sections, the polymer heat exchangers examined in this study are meant for antifouling and anti-corrosive applications. One such example is heat exchangers employed

for water treatment and desalination plants, particularly at high salinity levels. Here, the low surface energy of a polymer heat exchanger provides an antifouling advantage. Another example is heat exchangers employed in chemical processing involving acidic solutions and/or corrosive gases. Moreover, polymer heat exchangers offer a lightweight heat recovery solution for aerospace applications and evade radar detection for military applications. However, this study examined the polymer heat exchangers with air and water as the working fluids mainly due to their availability and compatibility with other experimental equipment, including pumps and mass flow meters. A desiccant-based humidity/oil separator was utilized to ensure that clean air was delivered to the test section. A submerged oil-to-air heater was used to heat the air stream to the desired temperature condition. The hot air leaving the heater was passed through the 3D-printed PHXs and thus cooled by the cold water stream flowing on the other side of the test heat exchangers.

As shown in Fig. 2, four T-type thermocouples (TCs) (Model: Reo-Temp F-M12T1SU4) with an accuracy of $\pm$ 0.2 °C were employed to measure the temperature difference across the HX test article. The pressure drop associated with the air flow through the 3D-printed PHXs was recorded by a differential pressure transducer (Model: Omega PX409-2.5DWU5V) with an accuracy of $\pm$ 1%. A data acquisition system (Model: Agilent 34972A LXI DAQ) was used to record temperature and pressure variations. The mass flow rate was measured with a Coriolis mass flow meter (Model: Bronkhorst Mini-CORI-FLOW-M13).

Table 1 lists the nominal operating conditions of the air and water flow streams. The inlet temperatures of the air and water streams were fixed at 45 °C and 23 °C, respectively. Performance of the PHXs was evaluated at an air mass flow rate range of 0.33 to 5.2 g/s for the plate-

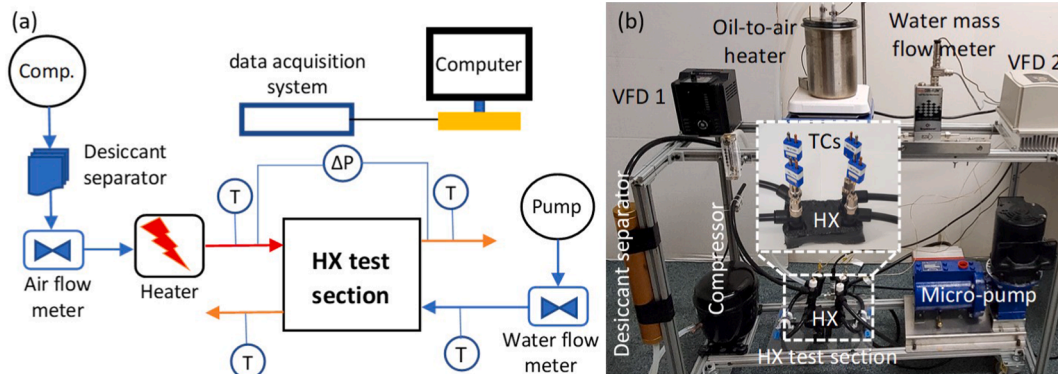**Fig. 2.** (a) A schematic, and (b) an image of the air-to-water HX test loop facility. Comp., VFD, HX, T/TC, and ΔP stand for compressor, variable frequency drive, heat exchanger, thermocouple, and differential pressure transducer, respectively.

Table 1
Nominal operating conditions.

	Plate-and-frame	Lung-inspired
Air inlet temperature (°C)	45	45
Water inlet temperature (°C)	23	23
Air Reynolds number	934 ~ 1467	951 ~ 1477
Air mass flow rate (g/s)	0.33 ~ 0.52	1.42 ~ 2.2
Characteristic length (mm)	1	2
Water mass flow rate (g/s)	0.21	0.91

and-frame PHXs and 1.42 to 2.2 g/s for the lung-inspired PHX. The mass flow rate of the cold water stream was remained constant at 0.21 and 0.91 g/s for the plate-and-frame and lung-inspired PHXs, respectively. It should be noted that thermal performances of the two PHX types were not examined at the same mass flow rate since the physical dimensions of the plate-and-frame (i.e., $10 \times 5 \times 0.5$ cm^3) and lung-inspired (i.e., $4.3 \times 4.1 \times 3.2$ cm^3) PHXs were not similar. Instead, the air/water mass flow rate was chosen in such a way that a similar Reynolds number range was ensured for the two PHX types. The hydraulic diameters of each PHX type were considered as the characteristic lengths in the Reynolds number calculations. The hydraulic diameter of the lung-inspired PHX was calculated based upon the minimum cross-sectional flow area available (i.e., the hexagon surface area available for the air flow stream in Fig. 1e).

3.2. Data reduction

The net thermal duty ($\dot{Q}$) exchanged by the PHXs is defined as the change in the sensible energies of the air and water streams as follows:

$$\dot{Q} = \dot{m}_{air}c_{p,air}\left(T_{air,in} - T_{air,out}\right) = \dot{m}_{water}c_{p,water}\left(T_{water,out} - T_{water,in}\right) \quad (1)$$

where $\dot{m}$ and c_p are mass flow rate and specific heat, respectively. The effectiveness of the PHXs is then defined as the ratio of net thermal duty to the maximum possible heat transfer rate ($\dot{Q}_{max}$) as follows:

$$\varepsilon = \frac{\dot{Q}_{ave}}{\dot{Q}_{max}} \quad (2)$$

where

$$\dot{Q}_{max} = (\dot{m}c_p)_{min}\left(T_{hot,in} - T_{cold,in}\right) \quad (3)$$

The maximum possible heat transfer rate between the hot and cold flow channels represents a hypothetical situation in which one fluid experiences the maximum possible temperature difference (i.e., $T_{hot,in} - T_{cold,in}$) in a counter-flow heat exchanger of infinite length. The maximum possible temperature difference is perceived by the fluid with the minimum heat capacity rate (i.e., $\dot{m}c_p$).

The logarithmic mean temperature difference (LMTD) of the PHXs is also defined as follows:

$$\Delta T_{lm} = (\Delta T_1 - \Delta T_2)/\ln(\Delta T_1/\Delta T_2) \quad (4)$$

where

$$\Delta T_1 = \left(T_{air,in} - T_{water,out}\right) \quad (5)$$

$$\Delta T_2 = \left(T_{air,out} - T_{water,in}\right) \quad (6)$$

Additionally, the *UA* value of the PHXs can be obtained as follows:

$$UA = \dot{Q}/\Delta T_{lm} \quad (7)$$

where U is the overall heat transfer coefficient and A is the heat transfer area.

3.3. Uncertainty analysis

The uncertainty associated with a function F which is a function of

$X_1, X_2, ..., X_n$ with uncertainties of $\delta X_1, \delta X_2, ... \delta X_n$ is calculated as follows [25]:

$$\delta F = \sqrt{\sum_i \left(\frac{\partial F}{\partial X_i}\right)^2 \delta_{X_i}^2} \quad (8)$$

Therefore, the uncertainty associated with the HX thermal duty ($\dot{Q}$) can be calculated as:

$$\frac{\delta \dot{Q}}{\dot{Q}} = \sqrt{\left(\frac{\delta \dot{m}_{air}}{\dot{m}_{air}}\right)^2 + \left(\frac{\delta(\Delta T_{air})}{\Delta T_{air}}\right)^2} \quad (9)$$

where ΔT is the temperature difference between the inlet and outlet ports. The uncertainty associated with the temperature difference can be calculated as:

$$\delta(\Delta T) = \sqrt{\delta T_{in}^2 + \delta T_{out}^2} \quad (10)$$

Using a similar approach, the uncertainties associated with effectiveness, *LMTD*, and *UA* can be estimated as follows:

$$\frac{\delta \varepsilon}{\varepsilon} = \sqrt{\left(\frac{\delta \dot{Q}_{ave}}{\dot{Q}_{ave}}\right)^2 + \left(\frac{\delta \dot{Q}_{max}}{\dot{Q}_{max}}\right)^2} \quad (11)$$

$$\delta(LMTD) = \sqrt{\left(\frac{1 - \frac{1}{R} - \ln(R)}{(\ln(R))^2} \cdot \delta(\Delta T_2)\right)^2 + \left(\frac{R - 1 - \ln(R)}{(\ln(R))^2} \cdot \delta(\Delta T_1)\right)^2} \quad (12)$$

$$\frac{\delta(UA)}{UA} = \sqrt{\left(\frac{\delta \dot{Q}_{ave}}{\dot{Q}_{ave}}\right)^2 + \left(\frac{\delta LMTD}{LMTD}\right)^2} \quad (13)$$

where R is $\Delta T_2/\Delta T_1$. Also, $\delta(\Delta T_1)$, and $\delta(\Delta T_2)$ can be calculated as follows:

$$\delta(\Delta T_1) = \sqrt{\left(\delta T_{air,out}\right)^2 + \left(\delta T_{water,in}\right)^2} \quad (14)$$

$$\delta(\Delta T_2) = \sqrt{\left(\delta T_{air,in}\right)^2 + \left(\delta T_{water,out}\right)^2} \quad (15)$$

Additionally, Table 2. shows the range and uncertainty of the main parameters.

4. Numerical simulation

Three-dimensional (3D) computational flow dynamic (CFD) simulations were conducted to further analyze experimental results. Fluid flow was considered to be steady-state, laminar, and incompressible. The continuity, momentum, and energy equations can be written as:

$$\frac{\partial u_i}{\partial x_i} = 0 \quad (16)$$

$$u_j \frac{\partial u_i}{\partial x_j} = -\frac{1}{\rho}\frac{\partial P}{\partial x_i} + \vartheta \frac{\partial u_i}{\partial x_j \partial x_j} \quad (17)$$

Table 2
Range and uncertainty of main parameters.

Variable	Range	Accuracy
Pressure	3 ~ 10 kPa	1%
Temperature	23 ~ 45 °C	0.2 °C
Water mass flow rate	–	0.5%
Air mass flow rate	35 ~ 55 SCFH	1 SCFH

$$u_j \frac{\partial T}{\partial x_j} = -\alpha \frac{\partial T}{\partial x_j \partial x_j} \qquad (18)$$

where u is the velocity, ρ is the density, P is the pressure, ϑ is kinematic viscosity, T is the temperature, and α is thermal diffusivity.

The CFD model was developed in the ANSYS Fluent software. First, the HX geometry was designed in the SpaceClaim module of the ANSYS Workbench. In the next step, the HX geometry was meshed in the Meshing module of the ANSYS Workbench. A boundary layer mesh with five layers at a growth ratio of 1.1 was used to capture the near-wall effects. Following a mesh independent study, a tetrahedral computational mesh type with an element size of 0.3 mm resulting in 4,509,867 computational cells was chosen. A schematic of the computational domain and a cross-sectional view of a representative generated mesh is shown in Fig. 3. The CFD simulations were conducted under a steady-state condition and a laminar flow regime. The inlet and outlet boundary conditions were set as mass flow inlet and outflow conditions, respectively. Additionally, no-slip and isolated boundary conditions are considered for internal walls and external surfaces of the HXs, respectively.

The CFD model was validated against the experimental results of the present study for the plate-and-frame PLA HX. The validated model was then employed to estimate the thermal conductivities of the metal-filled PLA and hi-k nylon-based PHXs. This was necessary as the effective thermal conductivity of the metal-filled PLA and hi-k polymer HXs might have been affected by the 3D-printing process. Table 3 lists thermo-physical properties of working fluids and different polymer filaments employed in the CFD modeling.

5. Results and discussion

5.1. Effective thermal conductivity of the 3D-printed polymer HXs

The effective thermal conductivity of the metal-filled and hi-k nylon-based polymer HXs could be affected by the 3D-printing process due to the re-arrangement of conductive additives during the material extrusion process. Therefore, several simulations at different thermal conductivities ranging from 0.1 to 300 W/m-K were conducted to examine the effect of thermal conductivity on the performance of the 3D-printed plate-and-frame PHXs. The simulations were performed at a nominal air mass flow rate of 0.42 g/s. The results were first validated at a thermal conductivity of 0.13 W/m-K for the PLA HX. Then, the simulation results were employed to estimate the effective thermal conductivities of the M−PLA and hi-k nylon-based PHXs.

Fig. 4 shows the effect of thermal conductivity on the thermal duty of the plate-and-frame HX design. At a fixed wall thickness of 1 mm, the thermal performance of the plate-and-frame HX increases as the thermal conductivity increases from 0.1 to 20 W/m-K. This is expected as a
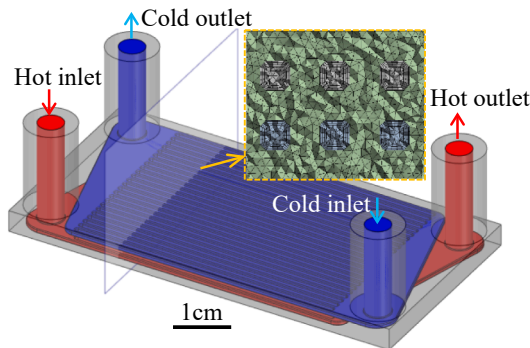
Table 3
Thermo-physical properties employed in the CFD simulations.

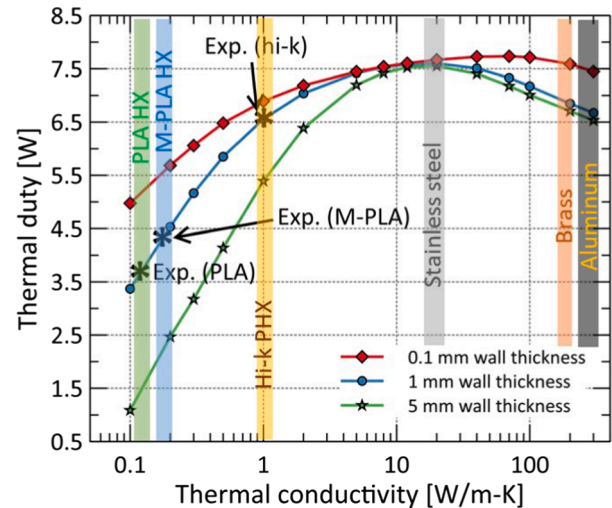|	Air	Water	PLA HX	M−PLA HX	hi-k nylon PHX
Density (kg/m³)	1.225	998.2	1240	1400	1450
Thermal conductivity (W/m-K)	0.0242	0.6	0.13	0.17	0.95
Specific heat (J/kg-K)	1006	4182	1800	2100	1100
Viscosity (kg/m-s)	1.789×10^{-5}	0.001003	–	–	–

Fig. 4. Effect of thermal conductivity and HX wall thickness on thermal duty of the plate-and-frame HX design.

material with a higher thermal conductivity allows a higher heat transfer rate between the cold and hot flow streams. Additionally, it is evident that the HX thermal duty is a strong function of the wall thickness (i.e., through-plane thermal resistance) at a low thermal conductivity range (e.g., 0.1 to 1 W/m-K). The thermal duty of the HX, however, decreases as the thermal conductivity increases from 20 to 300 W/m-K at the HX wall thickness of 1 mm. This is attributed to the axial (i.e., in-plane) heat conduction of the solid separating walls [26], which increases with thermal conductivity. The axial heat conduction is particularly important for 3D-printed HXs as the thickness of the separating walls is typically comparable to the hydraulic diameter. It should be noted that the through-plane wall thermal resistance weakens at high thermal conductivities.

To better illustrate the effect of solid thermal conductivity and axial heat conduction on the overall thermal performance of an HX module, three additional conceptual simulations at an extremely low thermal conductivity of 0.001 W/m-K, a thermal conductivity of 1 W/m-K, and an extremely high thermal conductivity of 1000 W/m-K were conducted (cf. Fig. 5). A similar counter flow plate-and-frame heat exchanger design shown in Fig. 3 with air as the working fluid for both hot and cold flow channels was considered. The length, width, and height of each hot or cold flow channel were 20, 1, and 1 mm, respectively. The inlet air velocity of each hot/cold channel was set at 1 m/s. The air inlet temperatures of the hot and cold flow channels were fixed at 100 and 20 °C, respectively. As shown in Fig. 5, when the solid thermal conductivity is extremely low (i.e., 0.001 W/m-K), the solid separating wall mainly acts as a thermal insulator with a small air temperature change of 2.5 °C for the hot and cold flow channels. Under this condition, the isothermal contours of the solid separating wall are parallel to the flow direction with minimum-to-zero axial heat conduction. Increasing the solid

Fig. 3. A schematic of the computational domain. The inset image shows a cross-sectional view of a representative generated mesh. The red, blue, and grey colors represent the air, water, and solid domains, respectively.
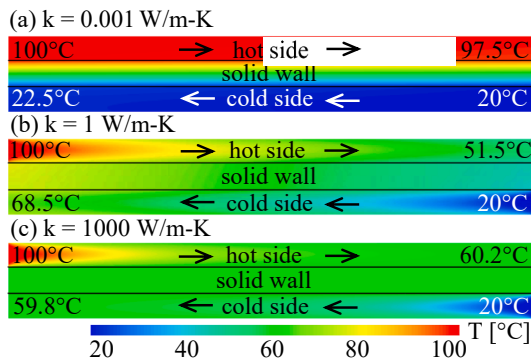
(a) k = 0.001 W/m-K

Fig. 5. Effect of axial heat conduction on the performance of a micro HX.

thermal conductivity to 1 W/m-K boosts the heat transfer rate between the hot and cold flow channels, thereby leading to an air temperature change of 48.5 °C for the hot and cold sides. When the solid thermal conductivity increases to 1000 W/m-K, the axial heat conduction maximizes. This results in a uniform temperature distribution for the solid separating wall that is equal to the average air inlet temperatures of the hot and cold sides (i.e., 60 °C). Consequently, the air temperatures of the hot and cold flow channels only change by 39.8 °C. In other words, under the simulated flow conditions and the physical HX dimensions considered, the heat transfer rate associated with an HX module with a solid thermal conductivity of 1000 W/m-K is lower than the thermal duty of an HX with a solid thermal conductivity of 1 W/m-K. This conclusion is consistent with that of Fig. 4.

Additionally, Fig. 4 shows that the simulation results well predict the experimentally measured thermal duty for the PLA polymer HX (i.e., PLA-HX) with a deviation of less than 3%. The PLA-HX shows a thermal duty of 3.7 W and an effectiveness of 40% at the nominal conditions. The thermal duties experimentally measured for the M−PLA and hi-k nylon-based PHXs are 4.2 and 6.5 W, respectively. A comparison between the experimental and simulation results suggests effective thermal conductivities of the M−PLA and hi-k nylon-based PHXs are 0.17 and 0.95 W/m-K, respectively. Therefore, the effective thermal conductivity of the hi-k nylon-based PHX is close to the through-plane thermal conductivity of the filament.

Furthermore, the high effective thermal conductivity of the hi-k nylon-based 3D-printed PHX enables high thermal duties (cf. Fig. 4) and exceptionally high effectiveness of 70–80% (as discussed later in Fig. 8) that are both comparable to those of metal-based HXs, including

stainless steel and aluminum materials. More importantly, the hi-k polymer is remarkably lighter than most metals (e.g., a density of 1450 kg/m³ for the hi-k polymer versus a density of 7500 kg/m³ for stainless steel), thereby offering a substantially lighter heat exchanging solution, particularly for antifouling and anti-corrosion applications.

5.2. Performance evaluation of plate-and-frame 3D-printed PHXs

Fig. 6 shows temperature contours of the PLA, M−PLA, and hi-k nylon-based 3D-printed PHXs in two horizontal cross-sectional mid-planes passing through the air (i.e., Fig. 6a, b, and c) and water (i.e., Fig. 6d, e, and f) flow streams. The inlet temperatures of the air and water flow streams are 45 °C and 23 °C, respectively. As shown, the manifold design allows an acceptable uniform flow and temperature distribution across different flow channels. The exit air temperatures of the PLA, M−PLA, and hi-k nylon-based PHXs are 36.1, 35.1, and 29.6 °C, respectively. This result clearly indicates a high thermal duty for the hi-k PHX design. Additionally, the high specific heat of water justifies the small temperature difference associated with the inlet and outlet of the water flow stream (i.e., 4.3 °C for PLA-HX and 7.4 °C for hi-k PHX).

Fig. 7a shows the thermal duty of the PLA, M−PLA, and hi-k nylon-based 3D-printed polymer HXs as a function of the air Reynolds (Re) number. To compare the thermal performances of the three plate-and-frame PHX designs at different thermal conductivities, the inlet air temperature, inlet water temperature, and inlet water mass flow rate were fixed at 45 °C, 23 °C, and 0.21 g/s, respectively (cf. Table 1). As evident, the simulation results well predict the experimental data at various air mass flow rates with a maximum deviation of less than 5%. At a fixed effective thermal conductivity, the thermal duty increases with the air Reynolds number. This is attributed to the air-side heat transfer coefficient, which increases at higher air mass flow rates. For instance, when the air-side Re number increases from 934 to 1467, the experimentally measured thermal duties of the PLA, M−PLA, and hi-k PHXs augment from 3.59, 3.95, and 5.77 W to 3.94, 4.38, and 7.23 W, respectively. It should be noted that the effect of the air mass flow rate on the thermal duty is magnified at higher effective thermal conductivities. At a low thermal conductivity (i.e., PLA and M−PLA polymers), the thermal duty of a 3D-printed PHX is mainly dominated by the conductive thermal resistance of the separating walls. At high thermal conductivities (i.e., hi-k nylon-based polymer), on the other hand, the thermal duty of a 3D-printed PHX is mostly governed by the convective resistance of the air flow stream as the conductive resistance of the separating walls weakens. Additionally, at a fixed Re number, the thermal duty of a 3D-printed PHX increases with the effective thermal
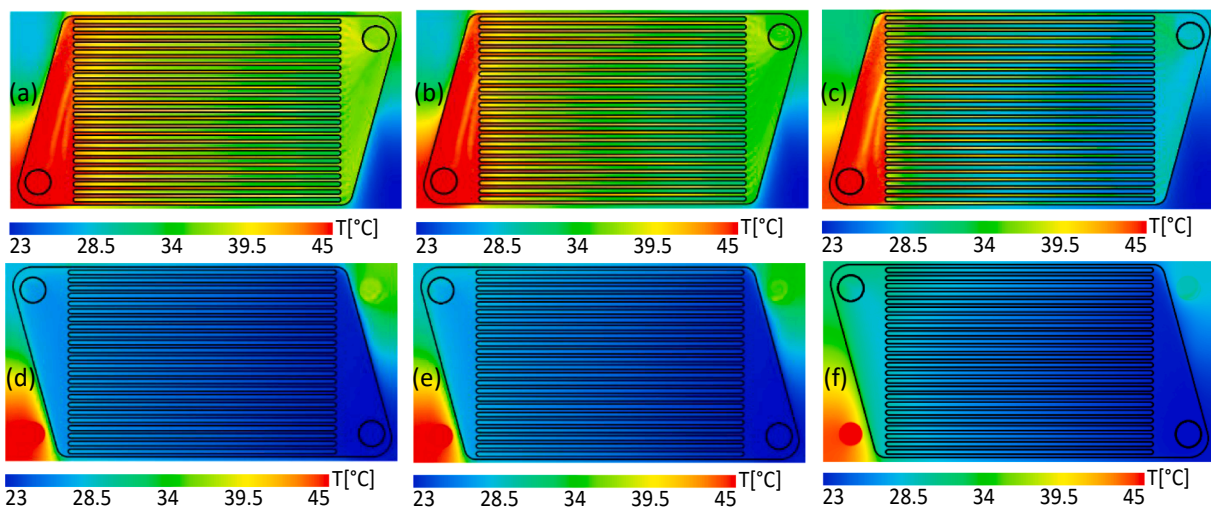

Fig. 6. Temperature contours of (a) PLA, (b) M−PLA, (c) hi-k, (d) PLA, (e) M−PLA, and (f) hi-k nylon-based PHXs in two horizontal cross-sectional mid-planes passing through the air (a, b, and c) and water (d, e, and f) flow streams.
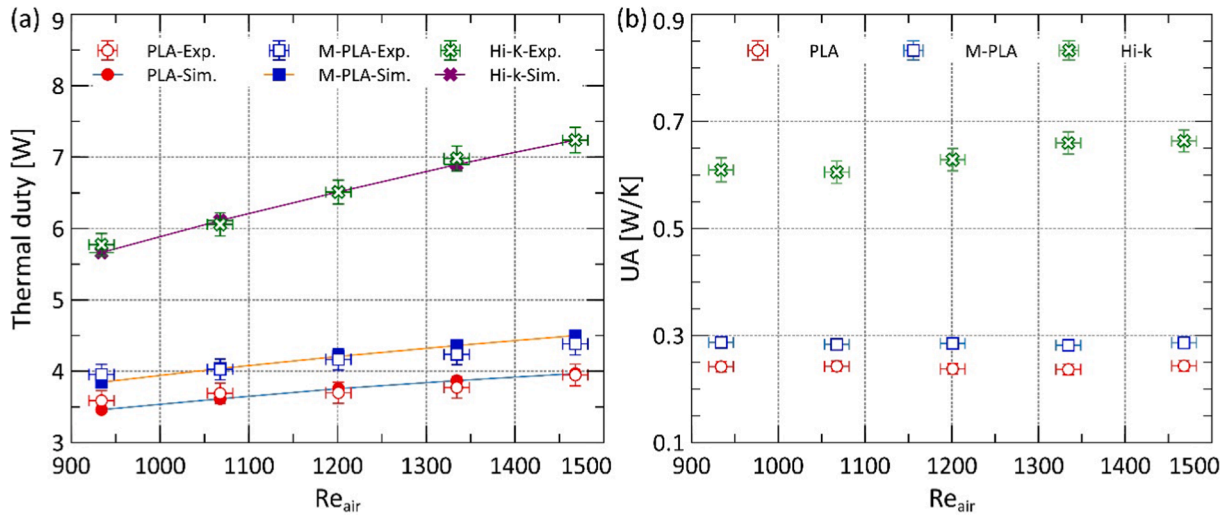
6

Fig. 7. Variations of (a) thermal duty, and (b) UA value versus air Re number for the PLA, M−PLA, and hi-k nylon-based 3D-printed PHXs.

conductivity. For example, at a Re number of 1200, thermal duty increases from 3.7 for the PLA-HX to 6.5 for the hi-k PHX.

Fig. 7b shows the experimentally measured UA values as a function of the air Re number for the three 3D-printed PHXs. At a fixed air Re number, a high thermal duty of the hi-k PHX leads to a small LMTD and thus a high UA value compared with the PLA and M-PLA PHXs. While the UA values of the PLA and M-PLA HXs are constant in the air mass flow rate explored, the UA value of the hi-k PHX slightly increases with the air mass flow rate. This clearly indicates that the thermal performance of the PLA and M-PLA HXs is mainly limited by the wall thermal resistance (i.e., no UA improvement by increasing the air mass flow rate). In contrast, the thermal performance of the hi-k PHX is no longer limited by the wall thermal resistance as its UA increases with the air mass flow rate.

Fig. 8 shows the experimentally measured effectiveness of the three 3D-printed plate-and-frame PHXs as a function of air Re number. The data shows that the HX effectiveness is inversely related to the air mass flow rate. The heat capacity rate (i.e., $\dot{m}c_p$) of the air stream is lower than that of the water stream. Therefore, the minimum heat capacity rate and thus the maximum possible heat transfer rate increase with the air mass flow rate. Although the thermal duty increases with the air mass flow rate, the effect of maximum possible heat transfer rate on HX

effectiveness is more pronounced, thereby decreasing the HX effectiveness at higher air flow rates. In other words, a lower fraction of the maximum possible heat transfer rate is exchanged at higher air mass flow rates. Additionally, at a fixed air Re number, the effectiveness of a 3D-printed PHX significantly increases with the thermal conductivity. Particularly, the hi-k nylon-based 3D-printed PHX demonstrates a high HX effectiveness range that is comparable with metal HXs. For instance, at a Re number of 1200, the hi-k 3D-printed PHX shows a high HX effectiveness of 70%, while the 3D-printed PLA HX only exhibits an HX effectiveness of 40%.

Fig. 9 shows the volume-based (VBPD) and mass-based power densities (MBPD) of the PHXs as a function of air Re number. The VBPD and MBPD are defined as the ratios of HX thermal duty to volume and mass of a PHX, respectively. As evident, the hi-k PHX offers higher VBPD and MBPD values compared with those of the PLA and M−PLA plate-and-frame PHX designs. In other words, a hi-k nylon-based PHX is lighter and more compact compared to its counterpart PLA and M−PLA PHX designs. For instance, at an air Re number of 1200, the VBPD and MBPD of the hi-k nylon-based PHX are 260 kW/m^3, and 147 W/kg, which are 56.3% and 75.8% improvement compared with the M−PLA HX design, respectively.

5.3. Performance evaluation of a lung-inspired hi-k nylon-based 3D-printed PHX

To fully leverage the design freedom offered by the 3D-printing process, a lung-inspired PHX was fabricated and experimentally examined. Fig. 10 shows the VBPD and pressure drop penalty of the hi-k nylon-based lung-inspired and plate-and-frame 3D-printed PHXs as a function of air Re number. As evident, the hi-k lung-inspired PHX offers a higher VBPD at a lower pressure drop penalty than that of the hi-k plate-and-frame PHX over a wide range of air Re numbers. This highlights the design advantages of the bronchi arrangement of the lung-inspired PHX, which allows higher thermal duties at lower pressure drop penalties.

As shown in Fig. 10a, the VBPD of the hi-k lung-inspired PHX is substantially higher than that of the hi-k plate-and-frame PHX. For instance, at an air Re number of 1200, the VBPD of the hi-k lung-inspired PHX is 522 kW/m^3, which is 100.8% higher than that of the hi-k plate-and-frame PHX demonstrating a VBPD of 260 kW/m^3. This is attributed to an improved flow distribution and thus an efficient heat transfer process offered by the lung-inspired HX design. Fig. 10b shows the air-side normalized pressure drop penalty of the hi-k lung-inspired PHX is significantly lower than that of the hi-k plate-and-frame PHX. For
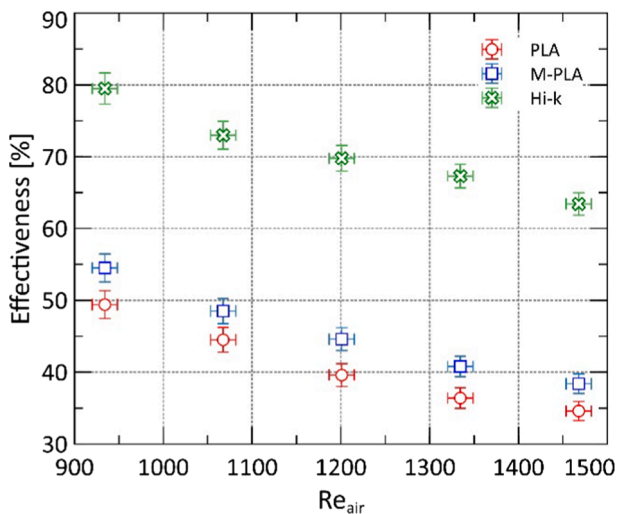

Fig. 8. Variations of the experimentally measured effectiveness versus air Re number for the PLA, M−PLA, and hi-k nylon-based 3D-printed PHXs.
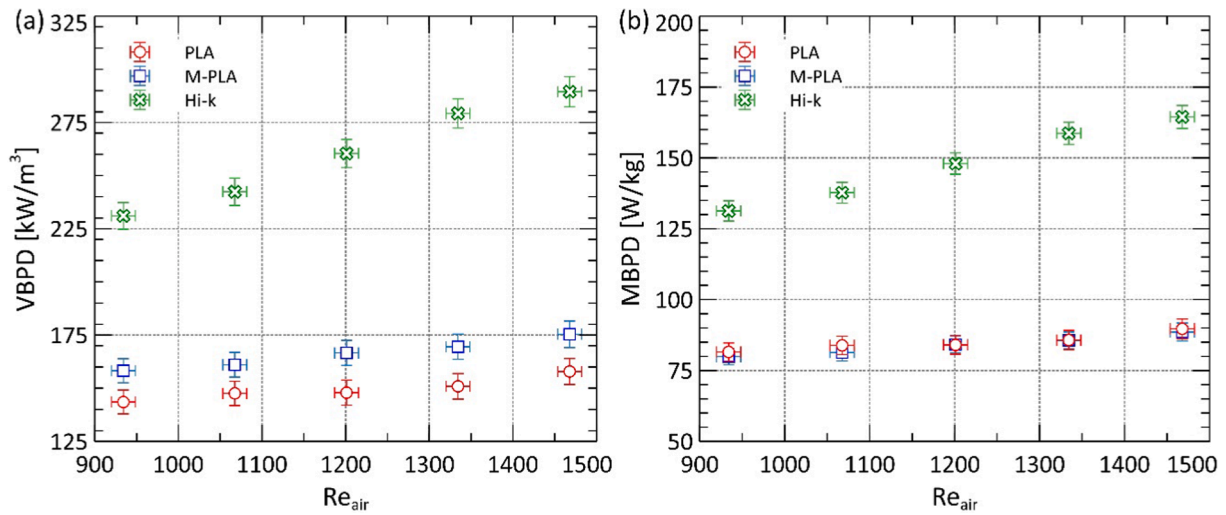
Fig. 9. Variations of (a) VBPD, and (b) MBPD as a function of air Re number for the PLA, M−PLA, and hi-k nylon-based 3D-printed PHXs.
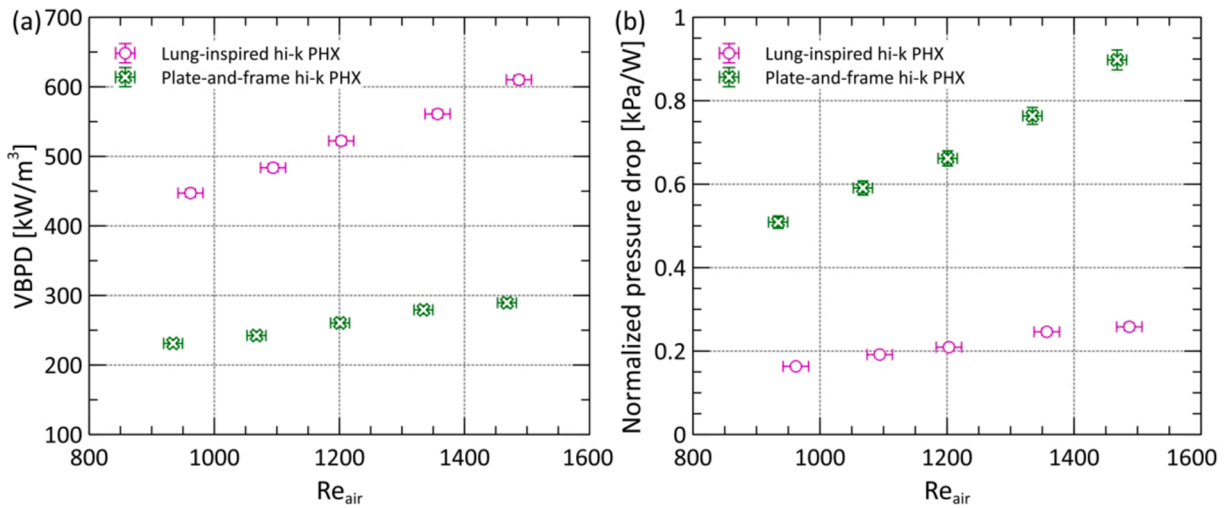

Fig. 10. Variations of the (a) VBPD, and (b) pressure drop penalty of the hi-k nylon-based lung-inspired and plate-and-frame 3D-printed PHXs as a function of air Re number.

example, at an air Re number of 1200, the air-side normalized pressure drop of the hi-k lung-inspired PHX is 0.21 kPa/W, which is 68% lower than that of the hi-k plate-and-frame PHX. Additionally, as expected, the air-side normalized pressure drop penalty increases with the air mass flow rates due to augmented frictional pressure losses. It should be noted that a normalized pressure drop penalty, defined as the air-side pressure drop divided by the HX thermal duty, was employed since the overall physical dimensions of the lung-inspired (i.e., $4.3 \times 4.1 \times 3.2$ cm^3) and plate-and-frame (i.e., $10 \times 5 \times 0.5$ cm^3) HXs were not the same. Additionally, Fig. S1 of the "supplementary materials" shows thermal duties and air-side pressure drop penalties of the hi-k lung-inspired and plate-and-frame PHXs as a function of air mass flow rate at a similar overall HX volume ($4.3 \times 4.1 \times 3.2$ cm^3 for the lung-inspired PHX, and $12.5 \times 5 \times 0.9$ cm^3 for the plate-and-frame PHX). Furthermore, it is worth noting that, at a water mass flow rate of 0.91 g/s, the water-side pressure drop penalties of the lung-inspired and plate-and-frame PHXs are 9 and 51 Pa, respectively.

Fig. 11 shows variations of the effectiveness of the hi-k nylon-based lung-inspired and plate-and-frame 3D-printed PHXs as a function of air Re number. As shown, the effectiveness of the hi-k lung-inspired PHX is higher than the hi-k plate-and-frame PHX. Particularly, the difference in the effectiveness becomes more significant at high air Re numbers. This
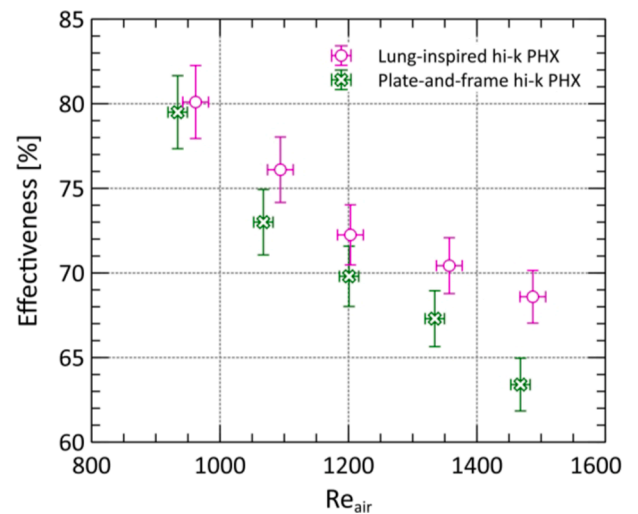

Fig. 11. Variations of the effectiveness of the hi-k nylon-based lung-inspired and plate-and-frame 3D-printed PHXs as a function of air Re number.

is because the lung-inspired design allows a volumetric distribution of one fluid network within and through the other network at high air mass flow rates.

Fig. 12 shows a comparison between VBPD and air-side normalized pressure drop values of the four 3D-printed PHXs examined. As evident, the hi-k nylon-based lung-inspired PHX demonstrates the highest values of the VBPD at the lowest normalized pressure drop penalty range. In contrast, the plate-and-frame PLA HX offers the lowest VBPD values at the highest normalized pressure drop penalty range. It is also clear that the thermo-hydraulic performance of the M−PLA HX is not meaningfully higher than the PLA polymer HX design. For a fixed HX topology (e. g., the plate-and-frame design), the hi-k PHX outperforms the low-k PLA PHX design. For a fixed thermal conductivity (e.g., hi-k polymer), the lung-inspired HX has a superior performance compared with its plate-and-frame counterpart. In other words, the performance of a polymer HX strongly depends on both material (i.e., thermal conductivity) and architecture (i.e., an optimum design with a minimal thermal resistance between hot and cold sides that might be only achievable through the 3D-printing process).

6. Conclusion

In summary, several 3D-printed polymer heat exchangers employing complex topologies and low-to-high thermal conductivities were experimentally examined. The through-plane leakage in thin 3D-printed polymer walls was found to be a major challenge associated with 3D-printed polymer heat exchangers. The leakage issue was overcome by in-situ infusion of an epoxy layer during the 3D-printing and a post-curing process. It was further observed that the effective thermal conductivity of the high thermal conductivity polymers is affected by the 3D-printing process due to the re-arrangement of conductive additives during the material extrusion process. A comparison between the experimental and simulation results suggested that the effective thermal conductivities of the metal-filled PLA and high thermal conductivity nylon-based 3D-printed polymer heat exchangers are 0.17 and 0.95 W/m-K, respectively. In other words, the effective thermal conductivity of a 3D-printed polymer heat exchanger is close to the through-plane thermal conductivity.

The effectiveness of the examined 3D-printed polymer heat exchangers made of low thermal conductivity polymers (i.e., PLA and metal-filled PLA) was found to vary between 35% and 55% at an air Re number range of 934 to 1467. However, the effectiveness of the 3D-printed polymer heat exchangers made of a high thermal conductivity polymer was determined to be considerably high in the range of 65% to 80%, which is comparable with that of a metal heat exchanger made of stainless steel and aluminum materials. Particularly, a high thermal conductivity nylon-based lung-inspired polymer heat exchanger design showed highly promising thermal performance values at reduced normalized pressure drop penalties and exceptionally high effectiveness of 70–80% that is comparable to that of metal-based heat exchangers. At an air Reynolds number of 1200, the volume-based power density of the high thermal conductivity lung-inspired polymer heat exchanger was 522 kW/m^3, which is a 101% improvement compared with a PLA plate-and-frame design. The results presented here suggest that the high thermal conductivity 3D-printed polymer heat exchangers employing complex internal heat transfer features could be considered as a highly promising alternative solution for lightweight applications and/or fouling/corrosive environments.

Declaration of Competing Interest

The authors declare that they have no known competing financial interests or personal relationships that could have appeared to influence the work reported in this paper.
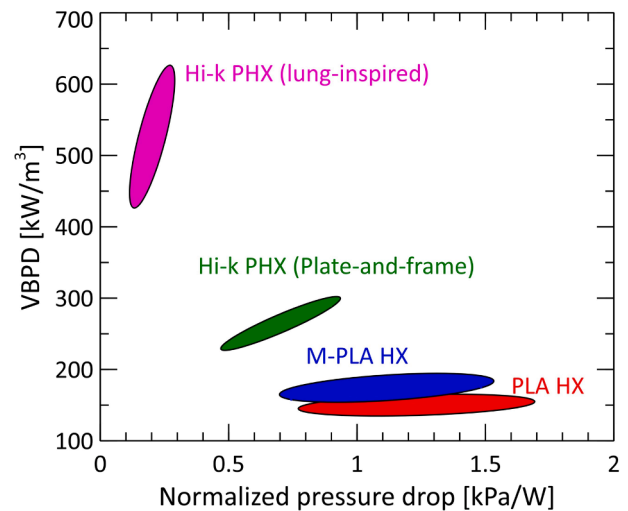

Fig. 12. A comparison between VBPD and air-side normalized pressure drop penalty of the four 3D-printed PHXs examined.

Appendix A. Supplementary material

Supplementary data to this article can be found online at https://doi.org/10.1016/j.applthermaleng.2021.117993.

References:

[1] M.V. Rane, Y.S. Padiya, Heat pump operated freeze concentration system with tubular heat exchanger for seawater desalination, Energy Sustain Dev 15 (2011) 184–191, https://doi.org/10.1016/j.esd.2011.03.001.

[2] H. Lim, U. Han, H. Lee, Design optimization of bare tube heat exchanger for the application to mobile air conditioning systems, Appl Therm Eng 165 (2020), 114609, https://doi.org/10.1016/j.applthermaleng.2019.114609.

[3] U. Puttur, M. Ahmadi, B. Ahmadi, S. Bigham, A novel lung-inspired 3D-printed desiccant-coated heat exchanger for high-performance humidity management in buildings, Energy Convers Manag 252 (2022), https://doi.org/10.1016/j.enconman.2021.115074.

[4] X. Zheng, X. Luo, J. Luo, J. Chen, Y. Liang, Z. Yang, et al., Experimental investigation of operation behavior of plate heat exchangers and their influences on organic Rankine cycle performance, Energy Convers Manag 207 (2020), 112528, https://doi.org/10.1016/j.enconman.2020.112528.

[5] J.S. Kwon, S. Son, J.Y. Heo, J.I. Lee, Compact heat exchangers for supercritical CO2 power cycle application, Energy Convers Manag 209 (2020), 112666, https://doi.org/10.1016/j.enconman.2020.112666.

[6] D.C. Deisenroth, R. Moradi, A.H. Shooshtari, F. Singer, A. Bar-Cohen, M. Ohadi, Review of Heat Exchangers Enabled by Polymer and Polymer Composite Additive Manufacturing, Heat Transf Eng 39 (2018) 1648–1664, https://doi.org/10.1080/01457632.2017.1384280.

[7] Sixel W, Liu M, Nellis G, Sarlioglu B. Cooling of Windings in Electric Machines via 3D Printed Heat Exchanger. 2018 IEEE Energy Convers. Congr. Expo., 2018, p. 229–35. https://doi.org/10.1109/ECCE.2018.8557845.

[8] M. Al-Zareer, Numerical Study of Flow and Heat Transfer Performance of 3D-Printed Polymer-Based Battery Thermal Management, Int J Heat Mass Transf 158 (2020), 119995.

[9] U. Han, H. Kang, H. Lim, J. Han, H. Lee, Development and design optimization of novel polymer heat exchanger using the multi-objective genetic algorithm, Int J Heat Mass Transf 144 (2019), 118589, https://doi.org/10.1016/j.ijheatmasstransfer.2019.118589.

[10] S. Shen, A. Henry, J. Tong, R. Zheng, G. Chen, Polyethylene nanofibres with very high thermal conductivities, Nat Nanotechnol 5 (2010) 251–255, https://doi.org/10.1038/nnano.2010.27.

[11] M.O. Khan, S.N. Leung, E. Chan, H.E. Naguib, F. Dawson, V. Adinkrah, Effects of Microsized and Nanosized Carbon Fillers on the Thermal and Electrical Properties of Polyphenylene Sulfide Based, Composites (2013), https://doi.org/10.1002/pen.

[12] Z. Han, A. Fina, Thermal conductivity of carbon nanotubes and their polymer nanocomposites : A review, Prog Polym Sci 36 (2011) 914–944, https://doi.org/10.1016/j.progpolymsci.2010.11.004.

[13] I. Krupa, I. Chod, Physical properties of thermoplastic / graphite composites 37 (2001) 2159–2168.

[14] J. Gu, Q. Zhang, J. Dang, J. Zhang, Z. Yang, Thermal Conductivity and Mechanical Properties of Aluminum Nitride Filled Linear Low-Density Polyethylene, Composites (2009), https://doi.org/10.1002/pen.

[15] W. Zhou, C. Wang, T. Ai, K. Wu, F. Zhao, H. Gu, Composites : Part A A novel fiber-reinforced polyethylene composite with added silicon nitride particles for

enhanced thermal conductivity, Compos Part A 40 (2009) 830–836, https://doi. org/10.1016/j.compositesa.2009.04.005.

[16] L. Chen, Z. Li, Z.-Y. Guo, Experimental investigation of plastic finned-tube heat exchangers, with emphasis on material thermal conductivity, Exp Therm Fluid Sci 33 (2009) 922–928.

[17] H. Glade, D. Moses, T. Orth, Polymer composite heat exchangers, in, Innovative Heat Exchangers. Springer (2017) 53–116.

[18] J. Cevallos, A. Bar-Cohen, D.C. Deisenroth, Thermal performance of a polymer composite webbed-tube heat exchanger, Int J Heat Mass Transf 98 (2016) 845–856.

[19] J. Sun, J. Zhuang, H. Jiang, Y. Huang, X. Zheng, Y. Liu, et al., Thermal dissipation performance of metal-polymer composite heat exchanger with V-shape microgrooves: A numerical and experimental study, Appl Therm Eng 121 (2017) 492–500, https://doi.org/10.1016/j.applthermaleng.2017.04.104.

[20] R. Trojanowski, T. Butcher, M. Worek, G. Wei, Polymer heat exchanger design for condensing boiler applications, Appl Therm Eng 103 (2016) 150–158, https://doi. org/10.1016/j.applthermaleng.2016.03.004.

[21] J. Jabbour, S. Russeil, M. Mobtil, D. Bougeard, M.-F. Lacrampe, P. Krawczak, High performance finned-tube heat exchangers based on filled polymer, Appl Therm Eng 155 (2019) 620–630.

[22] R.A. Felber, G. Nellis, N. Rudolph, Design and modeling of 3D-printed air-cooled heat exchangers, Int Refrig Air Cond Conf (2016).

[23] M.A. Arie, A.H. Shooshtari, R. Tiwari, S.V. Dessiatoun, M.M. Ohadi, J.M. Pearce, Experimental characterization of heat transfer in an additively manufactured

polymer heat exchanger, Appl Therm Eng 113 (2017) 575–584, https://doi.org/ 10.1016/j.applthermaleng.2016.11.030.

[24] M.A. Arie, D.M. Hymas, F. Singer, A.H. Shooshtari, M. Ohadi, An additively manufactured novel polymer composite heat exchanger for dry cooling applications, Int J Heat Mass Transf 147 (2020), 118889, https://doi.org/10.1016/ j.ijheatmasstransfer.2019.118889.

[25] B.N. Taylor, C.E. Kuyatt, NIST Technical Note 1297 Guidelines for Evaluating and Expressing the Uncertainty of NIST Measurement Results. NIST Tech Note 1297, 1994.

[26] T. Stief, O.U. Langer, K. Schubert, Numerical investigations of optimal heat conductivity in micro heat exchangers, Chem Eng Technol 22 (1999) 297–303, https://doi.org/10.1002/(SICI)1521-4125(199904)22:4<297::AID-CEAT297>3.0. CO;2-Y.

[27] M. Ahmadi, K.R. Gluesenkamp, S. Bigham, Energy-efficient sorption-based gas clothes dryer systems, Energy Convers Manag 230 (2021), https://doi.org/ 10.1016/j.enconman.2020.113763.

[28] B. Ahmadi, M. Ahmadi, K. Nawaz, A.M. Momen, S. Bigham, Performance Analysis and Limiting Parameters of Cross-flow Membrane-based Liquid-desiccant Air Dehumidifiers, International Journal of Refrigeration 132 (2021), https://doi.org/ 10.1016/j.ijrefrig.2021.09.010.

[29] S. Pinnu, S. Bigham, Multiple-effect desiccant-based zero liquid discharge desalination systems, Desalination 502 (2021), https://doi.org/10.1016/j. desal.2021.114942.